Spin-phonon couplings in transition metal complexes with slow magnetic relaxation

Duncan H. Moseley^a, Shelby E. Stavretis^a, Komalavalli Thirunavukkuarasu^{b,*}, Mykhaylo Ozerov^c, Yongqiang Cheng^d, Luke L. Daemen^d, Jonathan Ludwig^c, Zhengguang Lu^c, Dmitry Smirnov^c, Craig M. Brown^e, Anup Pandey^d, A. J. Ramirez-Cuesta^d, Adam C. Lamb^a, Mihail Atanasov^{f,g,*}, Eckhard Bill^{h,*}, Frank Neese^f, Zi-Ling Xue^{a,*}

Correspondence and requests for materials should be addressed to K.T. (email:

<u>komalavalli.thirunav@famu.edu</u>), M.A. (email: <u>mihail.atanasov@kofo.mpg.de</u>), E.B. (email: <u>eckhard.bill@cec.mpg.de</u>) or Z. X. (email: <u>xue@utk.edu</u>)

^a Department of Chemistry, University of Tennessee, Knoxville, Tennessee 37996, United States

^b Department of Physics, Florida A&M University, Tallahassee, Florida 32307, United States

^c National High Magnetic Field Laboratory, Tallahassee, Florida 32310, United States

^d Chemical and Engineering Materials Division, Spallation Neutron Source, Oak Ridge National Laboratory, Oak Ridge, Tennessee 37830, United States

^e Center for Neutron Research, National Institute of Standards and Technology, Gaithersburg, Maryland 20899, United States

f Max Planck Institute for Coal Research, Kaiser-Wilhelm-Platz 1, D-45470 Mülheim an der Ruhr, Germany

^g Institute of General and Inorganic Chemistry, Bulgarian Academy of Sciences, 1113 Sofia, Bulgaria

^h Max Planck Institute for Chemical Energy Conversion, Stiftstraße 34-36, D-45470, Mülheim an der Ruhr, Germany

Abstract

Spin-phonon coupling plays an important role in single-molecule magnets (SMMs) and molecular qubits. However, there have been few detailed studies of its nature. Here, we show for the first time distinct couplings of g phonons of $Co^{II}(acac)_2(H_2O)_2$ (acac = acetylacetonate) and its deuterated analogues with zero-field-split, excited magnetic/spin levels [Kramers doublet (KD)] of the S = 3/2 electronic ground state. The couplings are observed as avoided crossings in magnetic-field-dependent Raman spectra with coupling constants of 1-2 cm⁻¹. Far-IR spectra reveal the magnetic-dipole-allowed, inter-KD transition, shifting to higher energy with increasing field. DFT calculations are used to rationalize energies and symmetries of the phonons. A vibronic coupling model, supported by ab initio electronic structure calculations, is proposed to rationalize the behavior of the coupled Raman peaks. The current work spectroscopically reveals and quantitates the spin-phonon couplings in typical transiton metal complexes and sheds light on the origin of the spin-phonon entanglement.

Introduction

Transition metal complexes displaying slow magnetic relaxation are of great interest for possible use as single-molecule magnets (SMMs) and qubits¹⁻¹⁰. One current focus is to decrease the molecular size to a single metal center^{2,4,11}. To increase magnetic relaxation times, scientists have sought bistable complexes with large axial anisotropy¹⁻⁹ and large energy barriers for the magnetization reversal¹²⁻¹⁴. This is usually achieved by aiming for large, negative axial ZFS ($|D| \gg kT$) and vanishing rhombicity, E/D, rendering pure M_S functions and no direct magnetic-dipole transitions such as $M_S = -3/2 \rightarrow +3/2$ (S = 3/2 and D < 0). However, Gómez-Coca and coworkers recently reported that 1, a Kramers ion with large rhombic ZFS and significant g anisotropy,

behaves as an SMM in external magnetic fields $(D' = (D^2 + 3E^2)^{1/2} \approx 57 \text{ cm}^{-1}, E/D = 0.31)^{15}.$

Direct determination of large magnetic level separations (ZFS > 33 cm⁻¹) is a challenge⁴. Phonons are prevalent in the >15 cm⁻¹ region, making it difficult to distinguish them from magnetic peaks by IR or microwave spectroscopy¹⁶. Frequency-domain-Fourier-transform-terahertz-EPR spectroscopies (FD-FT-THz-EPR) has been used to detect 10-200 cm⁻¹ magnetic gaps^{10,17}. Far-IR has also been used to directly determine ZFS parameters¹⁸⁻²⁴, including the recent works by van Slageren and coworkers utilizing variable magnetic fields to identify magnetic peaks in SMMs^{21,22,25}.

Raman spectroscopy is seldom used to examine ZFS of transition metal complexes. In 1991, Gnezdilov and coworkers reported observation of ZFS transitions in $[Fe^{II}(H_2O)_6]SiF_6$ by Raman in magnetic fields^{4,26}. These results agree well with those from far-IR ($D = 11.78 \text{ cm}^{-1}$)²⁷, high-frequency electron paramagnetic resonance (HFEPR)²⁸ and frequency-domain-magnetic-resonance spectroscopy (FDMRS)²⁸. The authors attributed the Raman peaks in $[Fe^{II}(H_2O)_6]^{2+}$ to the presence of orbital angular momentum in the ZFS states. To our knowledge, Raman has not been used to probe molecular magnetism in other complexes, although electronic transitions have been probed²⁹⁻³⁵.

Spin-phonon coupling is often the mechanism of magnetic relaxation in SMMs and qubits $^{1-9,36}$. However, there is little understanding of these interactions, including their nature and magnitude. Phonons of SMM crystals include both intramolecular (or molecular) and lattice vibrations 37 . Recently, there has been a drive using theoretical models $^{38-40}$ to understand how phonons lead to relaxations in SMMs. Goodwin and co-workers have reported that $[Dy(Cp^{ttt})_2][B(C_6F_5)_4]$ ($Cp^{ttt} = 1,2,4$ -'Bu₃C₅H₂) displays magnetic hysteresis up to 60 K.- 40 . The magnetic relaxation is attributed to displacements primarily involving the C-H motions on the

Cp^{ttt} rings. A combination of experimental methods is needed to directly observe, and thus help understand, how phonons interact with unpaired electron spins. Recent experimental evidence in this area includes work performed by Rechkemmer and coworkers to observe spin-phonon couplings of two field-dependent absorptions of a Co^{II} SMM with far-IR spectroscopy²².

We report here our studies of Co(acac)₂(H₂O)₂ (1), Co(acac)₂(D₂O)₂ (1-d₄) and Co(acac-d₇)₂(D₂O) (1-d₁₈). Spin-phonon couplings have been probed by a combination of Raman and far-IR spectroscopies. With magnetic fields, the inter-Kramers transition moves and interacts with other phonons of g symmetry, rendering avoided crossings (coupling constants ≈ 1 -2 cm⁻¹). In Raman spectroscopy, phonon features of the coupled peaks are observed with applied magnetic fields. Far-IR spectroscopy reveals directly magnetic features of these coupled peaks. Periodic DFT calculations give computed energies, atomic displacements and symmetries of the phonons in 1-d₄ and 1-d₁₈ crystals. A vibronic model has been developed for the field-dependent Raman transitions in 1. In addition, *ab initio* calculations of the electronic structure in 1 reveal the origin of its ZFS.

Results

Structure and magnetic properties

Compound **1** is a high-spin, d^7 hexacoordinated Co^{II} complex with a pseudo-tetragonal structure (Figure 1a). Its crystal structure, determined by single-crystal X-ray diffraction at 100 K, shows C_{2h} molecular symmetry with equatorial and axial Co-O distances of 2.034, 2.040 and 2.157 Å, respectively. Crystal structure of **1-** d_{18} determined by powder neutron diffraction at 4 K allows the unambiguous location of D atoms (Supplementary Figures 1-2, Supplementary Table 1 and Supplementary Note 1). If the local symmetry around the Co^{II} ion is approximated to D_{4h} , the

ground electronic state is ${}^4A_{2g}$ (4A_g for C_{2h}). For high-spin, d^7 complexes in D_{4h} symmetry, ZFS leads to two KDs that, in the absence of rhombicity in zero field, can be labelled by $M_S = \pm 1/2$ and $\pm 3/2$. When D < 0, $E/D \approx 0$, the $M_S = \pm 3/2$ KD is the ground state with an easy axis of magnetization along the z-direction. For sufficiently large |D|, fields up to a few Tesla cannot mix the two KDs and induce any measurable magnetization in the x- or y-directions. In contrast, for D > 0 and $E/D \approx 0$ complexes (Figure 1b), the ground state KD $M_S = \pm 1/2$ is split into $M_S = -1$ 1/2 and +1/2 states by Zeeman splitting which is strongly direction-dependent. SMM behaviors in such complexes are not expected because transitions between these two states are spinallowed. Gómez-Coca and coworkers have shown that 1 behaves as an SMM (in external DC fields) despite its lower symmetry and dominating large rhombicity observed in EPR¹⁵. Magnetic susceptibility fittings revealed large ZFS $[D' = (D^2 + 3E^2)^{1/2} \approx 57 \text{ cm}^{-1}]^{15}$. EPR spectra showed typical rhombic effective g-values (2.65, 6.95, 1.83), rendering an easy axis of magnetization (along y), but this is far from the usual axial situation encountered for D < 0, $E/D \approx 0$, namely g' = (0, 0, g'z). The best global parametrization for EPR and susceptibility data was favored to have large rhombicity, E/D = 0.31, and moderate g anisotropy [for S = 3/2, g = (2.50, 2.57, 2.40)]. But in principle almost any value of E/D could be adopted, if the anisotropy of g is increased¹⁵. The effects are covariant, because both rhombicity and g anisotropy are mixing M_S functions, at least for finite fields, as visualized in Figure 1c. SH parameters cannot be deduced experimentally because no EPR spectrum is feasible for such highly excited " $M_S = \pm 3/2$ " KD in 1. Ab initio calculations yielded different values: D = 91.2, E = 10.1 cm⁻¹ (CASSCF) and D = 63.3, E = 9.3cm⁻¹ (CASPT2)¹⁵.

We chose 1 in part for the fact that it displays slow magnetic relaxation with $E/D \neq 0$, its reported magnetic separation $2D' \approx 114$ cm⁻¹ is relatively large and posed a challenge to measure

spectroscopically, and deuterated $1-d_4$ and per-deuterated $1-d_{18}$ could be prepared⁴¹.

Typical ZFS transitions between KDs in $\mathbf{1}$ (e.g., $M_S = -1/2 \rightarrow -3/2$) are magnetic-dipoleallowed by both symmetry and selection rules $(\Delta M_S = 0, \pm 1)^{42,43}$. (In the double group $D_{4h'}$, $M_S = \pm 1/2$ and $\pm 3/2$ KDs are represented by $E_{1/2,g}$ (Γ_6^+) and $E_{3/2,g}$ (Γ_7^+), respectively^{44,45}.) These transitions are therefore far-IR active^{14,18,19}. (In the point groups D_{4h} and C_{2h} , the magnetic dipole moment operators have the E_g , A_{2g} and $2B_g$, A_g symmetries, respectively, as the rotations, R_x , R_y and R_z .) The " $M_S = -1/2 \rightarrow +3/2$ " transition is ordinarily forbidden ($\Delta M_S = 2$). As discussed below, the large rhombic E value in $\mathbf{1}$ makes the $M_S = +3/2$ state contain the $M_S = -1/2$ character, thus rendering the " $M_S = -1/2 \rightarrow +3/2$ " transition magnetic-dipole-allowed. In other words, both " $M_S = -1/2 \rightarrow -3/2$ " and " $M_S = -1/2 \rightarrow +3/2$ " transitions in $\mathbf{1}$ are far-IR active. As vibronic analyses below demonstrate, spin-phonon couplings of the ZFS transition with g phonons make the two coupled peaks contain both magnetic and phonon features. In Raman spectra, the phonon excitations of the coupled peaks reveal spin-phonon couplings in variable magnetic fields. Far-IR spectra show directly the magnetic features of the coupled peaks.

Spin-phonon couplings in Raman spectroscopy

Raman spectra of 1, 1-d₄ and 1-d₁₈ under 0-14 T fields are given in Figures 2a-f. Figures 2a-b (1) show four Raman peaks in the energy range of 110–150 cm⁻¹, which are close to the energy estimated for the excited Kramers doublet at $2D' \approx 114$ cm⁻¹ ¹⁵. Interestingly, peak A at 116 cm⁻¹, which is the closest to 2D', is found to be slightly field-dependent, shifting monotonously to 119 cm⁻¹ at 14 T. Although this feature suggests a magnetic contribution, it is unlikely to be the ZFS transition between $\phi_{1,2}$ and $\phi_{3,4}$ levels of the KDs of 1 at zero field (Figures 1 and 3). The peak does not show Zeeman splitting and the shift rate of ~0.23 cm⁻¹/T corresponds to a very small

difference of effective g values, $\Delta g' \approx 0.5$ ($\mu_B = 0.4668$ cm⁻¹/T). We therefore infer that peak A is predominantly of phonon origin, and its change with field reflects the magnetic feature of the spin-phonon coupled peak. At 14 T, the phonon peak is still weakly coupled to the ZFS transition. Even more interesting is that peak C at 125 cm⁻¹ is field-independent below 4 T, but then attenuates with increasing field and shifts to higher energies, whereas in the same field range (4–8 T), peak B appears at ~120 cm⁻¹, gaining intensity with rising field and shifting to higher energy. Above ~8 T, peak B becomes field-independent just at the energy of the weakfield branch of peak C. This behavior has the appearance of an avoided crossing. Below, we will explain the effect by coupling of a phonon at 125 cm⁻¹ to the transition from the ground level ϕ_1 $|0\rangle$ to the excited level $\phi_4|0\rangle$, which is shifted by Zeeman effect across the phonon range (Figure 3). In this picture, the low-field branch of peak B is Raman-silent, as it is primarily a magnetic transition when the $\phi_4|0\rangle$ level is far from the phonon energy. However, it gains intensity at 4-8 T due to mixing of the phonon with the magnetic wave function. The high-field branch of B is a nearly pure phonon again (at 125 cm⁻¹). The shifting magnetic level at higher fields then generates a second avoided crossing with phonon peak D via the same mechanism.

Raman spectra of $1-d_4$ (Figures 2c-d) also exhibit spin-phonon couplings similar to those of 1, suggesting that deuteration of the water ligands in $1-d_4$ does not significantly alter magnetic peaks, phonons or their couplings in this region (110-140 cm⁻¹).

In Raman spectra of $1-d_{18}$ (Figures 2e-f), further deuteration has shifted many phonons compared to those of $1/1-d_4$. Phonon A and magnetic peak B appear to be coupled more strongly in $1-d_{18}$ than in $1/1-d_4$, such that both coupled peaks are observed at 0 T. With an applied field, A shifts to higher energy, eventually residing at 115 cm⁻¹ by 6 T. B loses intensity as it shifts at the rate of ~ 0.95 cm⁻¹/T and vanishes by 4 T, as there are no additional g phonons to couple with at

120-140 cm⁻¹ and 4-14 T (Figure 2e).

Raman peak positions in magnetic fields in Figures 2a-f are listed in Supplementary Table 2. The phonons that are coupled with the ZFS peak at 0 T, forming A and B in the spectra of 1, 1- d_4 and 1- d_{18} , are Raman-active. In the C_{2h} group, these phonons have A_g/B_g symmetry, as periodic DFT-VASP phonon calculations have shown in Supplementary Table 2.

Spin-phonon couplings and a vibronic model for the Raman spectra

The field-driven avoided crossings in the Raman spectra can be characterized by Figure 3^{48} . A simplified Hamiltonian for the coupling between magnetic $|\phi_i\rangle$ and phonon $|n\rangle$ states (Figure 3f) is given by the following 2×2 matrix Equation (1):

$$H = \begin{pmatrix} E_{\rm sp} & \Lambda \\ \Lambda & E_{\rm ph} \end{pmatrix} \tag{1}$$

where $E_{\rm sp}$ and $E_{\rm ph}$ are the expected energies of the magnetic and phonon excitations, respectively; Λ is the spin-phonon coupling constant. The energy gap between the two excited states $E_{\rm ph}-E_{\rm sp}$ is δ (Figure 3) which is not explicitly included in Equation (1).

Solving the matrix gives two eigenvalues E_{\pm} (with the associated avoided-crossing peaks $|\Psi_{\pm}\rangle$) in the secular Equation (2). An alternative, detailed expression of Equation (2) is given in Supplementary Note 2. Considering that Equation (2) involves Λ^2 , the sign of Λ may not be determined from the Raman spectra here.

$$\begin{vmatrix} E_{\rm sp} - E_{\pm} & \Lambda \\ \Lambda & E_{\rm ph} - E_{+} \end{vmatrix} = 0 \tag{2}$$

Upon coupling, $|\Psi_{+}\rangle$ shifts to higher E_{+} while $|\Psi_{-}\rangle$ shifts to lower E_{-} , as shown in Figure 3f⁴⁸. For example, both states $|\Psi_{\pm}\rangle$, giving rise to peaks A and B in the Raman spectra of **1-d₁₈** at 0 T (Figures 2e-f), contain magnetic and phonon features (Figure 3). Since the phonon here is Raman-active, the phonon portions of both A and B make the two peaks observable in the Raman spectra.

Equations (1-2) provide a model to understand the spin-phonon couplings in the Raman spectra (Figures 2a-f) and calculate the coupling constants, as discussed below. However, it should be pointed out that for the Hamiltonian in Equation (1), vibronic coupling in the ground KD is neglected. In principle, however, both the ground and excited KD states are involved in a transition, each has a spin and vibrational substate, which all may interact with each other. Thus, a more complete Hamiltonian should be at least a 6×6 , or better, an 8×8 matrix. In contrast, Equation (1) assumes that the ground KD state is not involved in spin-phonon coupling. In addition, this simple model assumes weak spin-phonon couplings. Therefore, terms higher than single phonon excitations are neglected. A more precise vibronic model for the spin-phonon couplings is presented in the Methods, Supplementary Figures 3-5 and in Supplementary Notes 3-4 and will be discussed below. Lastly, this model only considers coupling between the magnetic transition and one phonon, typically the phonon closest in energy to the ZFS transition. However, other distant g phonons may also be coupled to the magnetic transition, although weakly, thus taking the magnetic feature away.

Using Equation (2) to fit the spin-phonon couplings in Figures 2a-f yields the coupling constants |A| for each avoided crossing (Figure 4). |A| corresponds to roughly half the distance

between the peaks at their closest positions. The larger the coupling constant, the greater their repulsion (Figure 4).

We have developed a more detailed vibronic model to quantify the spin-phonon couplings in Figure 4. Complex 1 possesses a large rhombicity E/D. Parameters of the vibronic coupling model, extracted from the experimental field-dependent Raman spectra, turn out to be rather insensitive to the E/D ratio (Supplementary Table 3). Thus, we base qualitative discussions using our model on E = 0. Magnetic-field-dependent Raman spectra of 1 (Figures 2ab) consist of five branches A-E. For branches C-E, the regions at low and high fields show almost no field dependence. While not observed at low fields, B displays no field dependence at high field. A and C-E correspond to vibrations with estimated zero-field energies of $\hbar\omega_0 = 116$, $\hbar\omega_1 = 125$, $\hbar\omega_2 = 128$ and $\hbar\omega_3 = 139$ cm⁻¹. At intermediate magnetic fields, branches B-D display the slope of a magnetic-field-induced spin-transition as avoided crossings. There are three avoided crossing points between B-C, C-D and D-E at 7.64, 9.43 and 17.54 T with energies 125.05, 127.99 and 138.71 cm⁻¹, respectively. Here, magnetic excitations from the ground into the excited level would appear when no crossing (|A| = 0) is present. Energies of these unseen magnetic excitations increase with field and cross the three different vibrational levels (0 T) at $\hbar\omega_1 = 125$ (C), $\hbar\omega_2 = 128$ (D) and $\hbar\omega_3 = 139$ (E) cm⁻¹. $\hbar\omega_{1-3}$ are energies at the crossing points $[1/2(E_{sp} + E_{ph})]$, Equation (2) from the B-C, C-D and D-E couplings, respectively. Figure 5 displays simulations of the Raman transitions in the B||z field. The B||x and B||y field directions were fitted as well, but neither was a close match to the experimental results (Supplementary Figure 4). Analyses of the field-dependent Raman peaks were performed to potentially determine E/D. However, results of the analyses indicate that the derived parameters (Supplementary Table 3) are mostly insensitive to E/D. Discussions of the mechanism of the intensities in the fielddependent Raman spectra are given in Supplementary Note 5 and Supplementary Figures 6-7.

To the best of our knowledge, these are the first direct observation of spin-phonon couplings (as avoided crossings) in Raman spectra of a molecular compound and their quantification. Brinzari and coworkers have studied ferromagnetic, MOF (metal-organic framework)-like Co^{II}[N(CN)₂]₂ and also found a phonon-coupled, field-dependent transition in Raman spectra⁴⁹.

Spin-phonon couplings in far-IR spectroscopy

As discussed earlier^{14,18,19}, transitions between the two KDs are in general magnetic-dipoleallowed and therefore are potentially far-IR active. For the spin-phonon coupled states of **1**, **1-***d*₄ and **1-***d*₁₈ in Figure 3, the magnetic features of the transitions are far-IR active. In a diffuse reflectance measurement of a single crystal of **1-***d*₄ (Figure 6), the most significant difference between spectra of 0 and 16 T fields is a loss in absorption at ~115 cm⁻¹ (Figure 6a).

Normalizing these spectra (by dividing them by the 0 T spectrum to remove field-independent absorptions) reveals additional details (Figure 6a) which are further enhanced in a color-coded contour plot (Figure 6b).

The most remarkable feature is a (weak) field-dependent absorption, moving from 114 cm⁻¹ at 0 T to ~150 cm⁻¹ at 16 T (trace 1, Figure 6b). The shift rate of 2.25 cm⁻¹/T reveals a difference (or sum) of g' values of the initial and final levels of Δg ' ≈ 4.8 . From a comparison with the principal g' values obtained from the previous spin-Hamiltonian parametrization for $\mathbf{1}^{15}$ [g'i(1,2) = 2.65, 6.95, 1.83 for ϕ _{1,2} of the lower KD and g'i(3,4) = 2.34, 1.80, 6.63 for ϕ _{3,4} of the excited KD], we can infer in first order that the main observed field-dependent IR-peak (trace 1) may be from one of two possible transitions. The first is the ϕ ₁|0 $\rangle \rightarrow \phi$ ₂|0 \rangle transition with the

field in y-direction ($\Delta g' = 6.95 - 1.80 = 5.15$; green line II in Figure 7b); The second is the $\phi_1|0\rangle$ $\rightarrow \phi_4|0\rangle$ transition with the field in x-direction (sum of g' values: 2.65 + 2.34 = 4.99; red line I in Figure 7b). (At 5 K for the far-IR studies, only the $\phi_1|0\rangle$ should be thermally populated, at least for moderate to strong fields.) Corresponding simulations, using the full spin Hamiltonian (S =3/2) for the three principal field orientations (B||x, B||y, B||z) and for both magnetic transitions to the excited KD, are given in Figure 7. If trace 1 is the $\phi_1|0\rangle \rightarrow \phi_3|0\rangle$ transition (green line II in Figure 7b) with the field in y-direction (first possible transition above), another transition (green line I) to the right of trace 1 would be expected. However, no such trace is obvious in Figure 6b, suggesting that trace 1 is unlikely the $\phi_1|0\rangle \rightarrow \phi_3|0\rangle$ transition with the field in y-direction. If trace 1 is the $\phi_1|0\rangle \rightarrow \phi_4|0\rangle$ transition (red line I in Figure 7b) with the field in x-direction (second possible transition above), the $\phi_1|0\rangle \rightarrow \phi_3|0\rangle$ transition in x-direction (red line II in Figure 7b) to the left of trace 1 in Figure 6b is expected. Such behavior can be explained by the difference in the effective g values, $\Delta g' = 2.65 - 2.34 = 0.31$, which is still positive. In fact, traces 1 and 2 in Figure 6b are consistent with the analysis. Starting around 114 cm⁻¹ at B = 0, traces 1 and 2 are the $\phi_1|0\rangle \rightarrow \phi_4|0\rangle$ (red line I) and $\phi_1|0\rangle \rightarrow \phi_3|0\rangle$ (red line II) transitions, respectively. However, it should be noted that any such assignment is a simplification when the crystal orientation is not known, because other, off-axis orientations of the field may yield similar results.

Spin-phonon coupling, which was not included in the above analysis of Figure 6, should not change the general picture. However, it may explain the 'gaps' observed in the field-dependence of the $\phi_1|0\rangle \rightarrow \phi_4|0\rangle$ transition (trace 1). We suggest that the mixing of the $\phi_4|0\rangle$ state with IR-silent g phonons at the points of the avoided crossings reduces the absorption probability by 50%. As a result, rather sharp, distinct gaps occur for the magnetic transition (trace 1) at the phonon energies, as nicely observed around $\hbar\omega_1 = 125$, $\hbar\omega_2 = 128$ and $\hbar\omega_3 = 139$ cm⁻¹, which

have been assigned above to the g phonon peaks C, D, and E in the Raman spectra (Figures 2c-d).

Simulations in Figure 7 support the analysis discussed earlier that both $\phi_1 \rightarrow \phi_3$ and $\phi_1 \rightarrow \phi_4$ inter-KD transitions in 1 are magnetic-dipole allowed and are expected to be observable in far-IR. The two transitions, each in the x, y, z directions inside magnetic fields, lead to the expected shifting patterns of the six lines in Figure 7b. Most lines, except one, are blue-shifted to higher energies (Figure 7a). Thus, average far-IR spectra of a powder sample of 1 are expected to be blue-shifted and reveal the magnetic features of the spin-phonon coupled peaks. Indeed, the transmittance far-IR spectra of 1 (Supplementary Figures 8a-b and 9) show these features, except that the coupled peaks are not resolved as in the Raman spectra (Figures 2a-b). The far-IR transmittance spectra of a powder sample of 1- d_4 (Supplementary Figures 8c-d and 10) are also consistent with the spin-phonon coupling and features of the far-IR spectra of the single crystal of 1- d_4 (Figure 6). Far-IR transmittance of 1- d_{18} reveals similar features in Supplementary Figures 8e-f and 11.

Additional discussions of the far-IR spectra are given in Supplementary Note 6. In the far-IR spectra of $1-d_4$, there are four u phonons between 115 and 143 cm⁻¹ (Supplementary Table 2). Their symmetries have been assigned by the VASP calculations discussed below. No observed coupling between these u phonons and the ZFS peak is found in far-IR spectra.

The results here from the Raman and far-IR spectroscopies show that only the couplings of the ZFS transition to the g phonons in 1, 1- d_4 and 1- d_{18} are observed in Raman spectra. Far-IR spectra in the current work do not reveal couplings to the u phonons. Work on the transition matrix in the future may provide an understanding. It should be noted, however, that pattern of the couplings is limited to the current complexes. Additional work on other complexes,

especially those with different symmetries, is needed to have a comprehensive understanding of the couplings.

Periodic DFT phonon calculations and comparisons with experiments

Phonon modes for C_{2h} **1-** d_4 and **1-** d_{18} are calculated by VASP (Supplementary Table 2) and show atomic displacements with contributions from both external (lattice) and internal modes. In the region of interest here, ~115 cm⁻¹, vibrations are not localized but involve atomic displacements of the whole molecule, as demonstrated in Supplementary Movies 1-5. The modes with the largest spin-phonon coupling constant |A|, E of $1/1-d_4$ (Supplementary Movie 4 for phonon E of $1-d_4$) and A of $1-d_{18}$ (Supplementary Movie 5), have greatly mismatched vector magnitudes of the equatorial O atoms, leading to a larger net change in this bond angle (Supplementary Table 6). These vibrations significantly distort the first coordination sphere and perhaps lead to the larger |A|. Therefore, we rationalize that, if these phonons are involved in magnetic relaxation, the O-Co-O equatorial-bond-angle distortion plays a key role in the spin reversal. These spin changes of the excited KD is of prime importance for the magnetic relaxation at elevated temperatures where the excited KD is populated. Likewise, low-energy phonons (not included in Supplementary Table 2) are responsible for the low-temperature shortcut of the relaxation time. These effects are beyond the scope of the present work. Modes C and D 1-d₄ (Supplementary Movies 2 and 3, respectively) have less distortion of the O-Co-O equatorial bond angle and therefore, we reason, do not couple as strongly with spin. These findings are in line with recent calculations of spin-phonon couplings in [(tpa^{Ph})Fe]⁻ [H₃tpa^{Ph} = tris((5-phenyl-1*H*-pyrrol-2vl)methyl)amine] by Lunghi and coworkers demonstrating that the vibrations perturbing the bending angle of the equatorial N atoms coordinated to the Fe^{II} ion are strongly coupled to the

spin³⁸.

Additional results of the phonon calculations, including distortion of the O-Co-O bond angle in the equatorial plane compared with the spin-phonon coupling constants |A| (Supplementary Table 6), are given in Supplementary Figures 12-13 and Supplementary Note 7. Supplementary Movie 1 for phonon A of **1-d₄** is also provided.

Origin of ZFS in 1 analyzed by ab initio calculations

Although **1** has been studied as a model complex^{15,50,51}, its ZFS origin is not clear. Electronic structure of **1** has been reconsidered using multireference *ab initio* calculations in close relation and comparison with two basic experimental studies^{15,51}, including the single-crystal EPR work by Bencini and coworkers⁵¹, in order to probe the origin. Lohr and coworkers have calculated the electronic structure of **1** with descending crystal field symmetry from octahedral to orthorhombic and used the results to obtain magnetic properties⁵⁰. Details of the current electronic structure calculations and comparisons with experimental results are given in Supplementary Figures 14-18, Supplementary Tables 7-8 and Supplementary Note 8.

According to the orbital energy diagram, $d_{x'z',y'z'} < d_{x'^2-y'^2}$ (Supplementary Figure 17), the ${}^4T_{1g}$ state of a high-spin octahedral Co^{II} complex undergoes a D_{4h} splitting into an ${}^4A_{2g}$ ground state and an 4E_g excited state. When the symmetry is lowered to D_{2h} and C_{2h} , 4E_g (D_{4h}) state undergoes further splitting. Energies of all ten S = 3/2 states and the effect of symmetry lowering are listed in Supplementary Table 7. The sublevels of ${}^4T_{1g}$ are well separated from the excited ${}^4T_{2g}$ levels with the overall splitting of the ${}^4T_{1g}$ level about twice the effective Co^{II} spin-orbit coupling (SOC) parameter (530 cm⁻¹).

Ab initio NEVPT2 calculations indicate that the splitting between the two KDs is 169.8

cm⁻¹, with the SOC-excited states stemming from the ${}^4E_{\rm g}$ levels to be at 884.1, 1144.7, 1481.9 and 1616.2 cm⁻¹, showing that there are no other excited states in the vicinity of the lowest excited level at 169.8 cm⁻¹. The computed $g_{x'}$, $g_{y'}$ and $g_{z'}$ values of the lowest KD are 6.846, 3.745 and 1.864, respectively.

From the D eigenvalues, we deduce D and E, D = 3/2 $D_{zz} = 81.4$ and $E = (D_{xx} - D_{yy})/2 = 14$ cm⁻¹ and E/D = 0.17. At the temperatures available to probe the magnetic properties by magnetic susceptibility, field-dependent magnetization and EPR, there is no appreciable population of the lowest excited KD state.

High-quality single EPR spectra have been deduced from a single-crystal, X-band study reporting g-values of 2.74, 6.84 and 1.88⁵¹. They compare in magnitude and direction well with the computed results (*vide supra*). Parameters of the spin-Hamiltonian deduced from an interpretation of *both* the low-temperature magnetic data and the EPR spectra have been used to deduce the principal values of the gyromagnetic tensor and the zero-field splitting¹⁵: D = 57.0, E/D = 0.31, $g_x = 2.50$, $g_y = 2.57$, $g_z = 2.40$ and $g'_x = 2.65$, $g'_y = 6.95$, $g'_z = 1.83$. They are again compatible with the computed results in Supplementary Table 8.

Current studies spectroscopically reveal and quantitate the spin-phonon couplings in a typical Kramers complex. These studies offer a unique look at how spectroscopies can be utilized to study spin-phonon couplings in molecular complexes. The work here provides a rare case to compare Raman and far-IR spectroscopies and shows how the two, working together with *ab initio* and periodic DFT phonon calculations, reveal the spin-phonon couplings. In addition, the vibronic model developed to understand the Raman data sheds light on the origin of spin-phonon entanglement. At different external magnetic fields, the ZFS peak couples to different phonons. The spectroscopies at magnetic fields >14 T may reveal further couplings of

the ZFS transition with other phonons not observed in the current work. These experiments confirm the importance of obtaining spin-phonon coupling constants to understand how the lattice promotes relaxation at elevated temperatures. Importantly, spin-phonon coupling is not exclusively a phenomenon in SMMs, but is observed in a variety of magnetic materials.

We expect that the Raman and far-IR spectroscopies could be used to probe f complexes and d complexes with the first-order orbital momentum. Electric-dipole or magnetic-dipole transitions between states may be observed in far-IR, IR or UV-visible spectroscopies⁵². SOC is generally larger than the effect of the crystal field for f complexes⁵³. States in f complexes thus have both orbital and spin features as a result of the coupling. Transitions between these states are thus also Raman-active, following the electronic Raman selection rules ($\Delta J \leq 2$, $\Delta L \leq 2$, $\Delta S = 0$)⁵⁴. This is in contrast to the current work on a d complex with quenched first-order orbital angular momentum, where the Raman peaks are phonon parts of spin-phonon coupled peaks and the spin parts are from the ZFS transition.

Methods

Synthesis of 1, $1-d_4$ and $1-d_{18}$

The following chemicals were used as received: Co(acac)₂ (Alfa Aesar), CoCl₂ (Alfa Aesar), acetylacetone (Fisher Scientific), K₂CO₃ (Sigma-Aldrich), D₂O (99.9% D, Cambridge Isotope Laboratories) and CH₂Cl₂ (Fisher Scientific, Certified ACS grade). Dimethylformamide (Fisher Scientific, Certified ACS grade) was dried using 5 Å molecular sieves.

Complex 1 was synthesized according to the method of Ellern and coworkers⁴¹ by dissolving the anhydrous tetramer Co(acac)₂ in DMF and adding H₂O to the dark purple solution. The solution lightened and pinkish-orange crystals formed. Replacing H₂O with D₂O yielded the

partially deuterated compound **1-***d*₄. Larger crystals were obtained when less H₂O/D₂O was used and allowed to crystallize at -35 °C.

Deuterated acetylacetone was prepared by the method of Frediani *et al.*⁵⁶. Acetylacetone (10 mL, 9.8 g, 0.098 mol) was added to 100 mL of D₂O and 1 g of K₂CO₃ into a Schlenk flask under nitrogen gas. The solution was refluxed under nitrogen overnight at 120 °C. After cooling the solution to room temperature, the organic product, deuterated acetylacetone, was extracted from the aqueous layer using CH₂Cl₂. Solvent was then removed in vacuo. Deuteration level was analyzed using DART (Direct Analysis in Real Time) mass spectrometry. The process was repeated a second time with another 100 mL of D₂O to give acetylacetone-*d*₈ (91% D; 100% yield).

Co(acac- d_7)₂(D₂O)₂ (**1-d_{18}**) was synthesized by mixing D₂O (20 mL, 22 g, 1.1 mol), acetylacetone- d_8 (2.5 mL, 2.4 g, 22 mmol) and CoCl₂ (0.30 g, 2.3 mmol). K₂CO₃ (3.12 g) was qualitatively added to dissolve the acetylacetone- d_8 until traces of an amorphous solid began to precipitate. The solution was filtered, followed by further addition of K₂CO₃ until polycrystalline **1-d_{18}** formed. The mixture was filtered and washed with D₂O to give **1-d_{18}** (0.45 g, 62% yield based on CoCl₂).

Far-IR and Raman spectroscopies under variable magnetic fields

Far-IR and Raman spectroscopic studies were conducted at the National High Magnetic Field Laboratory (NHMFL) at Florida State University. For reflectance far-IR spectra of **1-d**₄, an unoriented single crystal was used. For transmittance far-IR spectra, the powdered samples were mixed with eicosane and pressed into pellets that were approximately 1 mm thick. Spectra were collected at 5 K using a Bruker Vertex 80v FT-IR spectrometer coupled with a superconducting

magnet (SCM) with fields up to 17.5 T.

Raman samples were prepared with unoriented single crystals of **1** and **1**-*d*₄ and powders of **1**-*d*₁₈. Data were collected by a backscattering Faraday geometry using a 532 nm laser at a 14 T SCM in the Electron Magnetic Resonance (EMR) facility and an 18 T SCM in the DC Field facility. Crystals of samples were cooled at 5 K (14 T) and 1.5 K (18 T). Collected scattered light was guided via an optical fiber to a spectrometer equipped with a liquid-nitrogen-cooled CCD camera.

Vibronic model for the magnetic-field-dependent Raman spectra of 1

The vibronic coupling model here, an extension of that in ref. 22 applied for a single mode, accounts for three intervening vibrations coupling to the $M_S = \pm 1/2$, $\pm 3/2$ sublevels of S = 3/2 spin. The Hamiltonian of the spin-phonon coupled system of a spin (S) with three vibrations is composed of three terms representing the spin (\hat{H}_S) , the phonons (\hat{H}_{vib}) and the spin phonon coupling (\hat{H}_{S-vib}) :

$$\hat{H}_{eff} = \hat{H}_S + \hat{H}_{vib} + \hat{H}_{S-vib} \tag{3}$$

The spin-Hamiltonian for an S = 3/2 spin is:

$$\hat{H}_{S} = D(\hat{S}_{z}^{2} - 5/4) + E(\hat{S}_{x}^{2} - \hat{S}_{y}^{2}) + \beta_{B}g_{x}B_{x}\hat{S}_{x} + \beta_{B}g_{y}B_{y}\hat{S}_{y} + \beta_{B}g_{z}B_{z}\hat{S}_{z}$$
(4)

For the three vibrations (i = 1,2,3):

$$\hat{H}_{vib} = \sum_{i} \hbar \omega \left(n_i + 1/2 \right) \tag{5}$$

the spin-phonon coupling Hamiltonian is:

$$\hat{H}_{S-vib} = \sum_{i} (\partial E / \partial Q_i)_o Q_i (\hat{S}_x^2 - \hat{S}_y^2) + (\partial D / \partial Q_i)_o Q_i (\hat{S}_z^2 - 5/4)$$
(6)

With $|M_s=\pm 3/2\rangle$ and $|M_s=\pm 1/2\rangle$ as the basis functions for the spin-sublevels of the S = 3/2 spin and $\chi_{n_i}(Q_i)$, i=1,2,3 as the harmonic oscillator wavefunctions for the three interacting modes, the spin-phonon wavefunction $|\Psi_{S-vib,k}\rangle$ can be expanded into a series of products as spin-sublevels and the three vibrational functions:

$$\left|\Psi_{S-vib,k}\right\rangle = \sum_{M_S=\pm 1/2,\pm 3/2} \sum_{n_1,n_2,n_3} c_{k,M_s,n_1,n_2,n_3} \left|M_s\right\rangle \chi_{n_1}(Q_1) \chi_{n_2}(Q_2) \chi_{n_3}(Q_3)$$
(7.1)

Under the assumption of a weak spin-phonon coupling, one can restrict the calculations to the ground and lowest phonon excited states: $n_i = 0,1$ leading to the following set non-vanishing product functions in the expansion of Equation (7.1):

$$|M_{S}\rangle\chi_{n_{1}}(Q_{1})\chi_{n_{2}}(Q_{2})\chi_{n_{3}}(Q_{3}):|3/2\rangle\chi_{0}(Q_{1})\chi_{0}(Q_{2})\chi_{0}(Q_{3}) = (3/2,0,0,0)$$
(7.2)

$$|1/2\rangle\chi_0(Q_1)\chi_0(Q_2)\chi_0(Q_3) = (1/2,0,0,0)$$
 (7.3)

$$|-1/2\rangle\chi_0(Q_1)\chi_0(Q_2)\chi_0(Q_3) = (-1/2,0,0,0)$$
 (7.4)

$$\left| -3/2 \right\rangle \chi_0(Q_1) \chi_0(Q_2) \chi_0(Q_3) = (-3/2,0,0,0) \tag{7.5}$$

$$|3/2\rangle\chi_1(Q_1)\chi_0(Q_2)\chi_0(Q_3) = (3/2,1,0,0)$$
 (7.6)

$$|1/2\rangle\chi_1(Q_1)\chi_0(Q_2)\chi_0(Q_3) = (1/2,1,0,0)$$
 (7.7)

$$\left|-1/2\right\rangle \chi_1(Q_1)\chi_0(Q_2)\chi_0(Q_3) = (-1/2,1,0,0)$$
 (7.8)

$$\left| -3/2 \right\rangle \chi_1(Q_1) \chi_0(Q_2) \chi_0(Q_3) = (-3/2,1,0,0) \tag{7.9}$$

$$|3/2\rangle\chi_0(Q_1)\chi_1(Q_2)\chi_0(Q_3) = (3/2,0,1,0)$$
 (7.10)

$$|1/2\rangle\chi_0(Q_1)\chi_1(Q_2)\chi_0(Q_3) = (1/2,0,1,0)$$
 (7.11)

$$\left|-1/2\right\rangle \chi_0(Q_1)\chi_1(Q_2)\chi_0(Q_3) = (-1/2,0,1,0) \tag{7.12}$$

$$\left| -3/2 \right\rangle \chi_0(Q_1) \chi_1(Q_2) \chi_0(Q_3) = (-3/2,0,1,0) \tag{7.13}$$

$$|3/2\rangle\chi_0(Q_1)\chi_0(Q_2)\chi_1(Q_3) = (3/2,0,0,1)$$
 (7.14)

$$|1/2\rangle\chi_0(Q_1)\chi_0(Q_2)\chi_1(Q_3) = (1/2,0,0,1)$$
 (7.15)

$$|-1/2\rangle\chi_0(Q_1)\chi_0(Q_2)\chi_1(Q_3) = (-1/2,0,0,1)$$
(7.16)

$$\left| -3/2 \right\rangle \chi_0(Q_1) \chi_0(Q_2) \chi_1(Q_3) = (-3/2,0,0,1) \tag{7.17}$$

Within this basis, the non-vanishing matrix elements of the spin-phonon coupling Hamiltonian are given by:

$$\left\langle \pm \frac{3}{2}, 1 \middle| (\partial E / \partial Q_i)_o Q_i (\hat{S}_x^2 - \hat{S}_y^2) \middle| \mp \frac{1}{2}, 0 \right\rangle = \sqrt{\frac{3}{2}} (\partial E / \partial Q_i)_o = E_i$$
 (8)

$$\left\langle \pm \frac{3}{2}, 1 \middle| (\partial D / \partial Q_i)_o Q_i (\hat{S}_z^2 - 5 / 4) \middle| \pm \frac{3}{2}, 0 \right\rangle = \frac{1}{2\sqrt{2}} (\partial D / \partial Q_i)_o = D_i$$
 (9)

$$\left\langle \pm \frac{1}{2}, 1 \middle| (\partial D / \partial Q_i)_o Q_i (\hat{S}_z^2 - 5 / 4) \middle| \pm \frac{1}{2}, 0 \right\rangle = -\frac{1}{2\sqrt{2}} (\partial D / \partial Q_i)_o = -D_i$$
 (10)

resulting in Supplementary Eqs. (4-6).

Calculations of the electronic structure in 1

The geometry of the first coordination sphere of Co^{II} including only the donor oxygen atoms is D_{4h} , represents a tetragonally elongated octahedron with two axial Co-O bonds to two water molecules (2.199 Å) and four equatorial Co-O bonds (2.05 Å) to two acac ligands. The crystallographic symmetry is C_{2h} (Supplementary Figure 14). For spin-Hamiltonian parameters from *ab initio* NEVPT2 calculations, SOC, along with quasi-degenerate perturbation theory accounted for using all 10 S = 3/2 and 40 S = 1/2 non-relativistic states (roots) of the d^7 Co^{II} configuration, was used to compute the ground and excited magnetic sublevels and to access the parameters of the spin Hamiltonian in Equation (11).

$$\hat{H}_{S} = D\left[\hat{S}_{z}^{2} - \frac{1}{3}S(S+1) + \frac{E}{D}(\hat{S}_{x}^{2} - \hat{S}_{y}^{2})\right] + \mu_{B}\vec{B} \cdot g \cdot \hat{\bar{S}}$$
(11)

The ground ${}^4A_{\rm g}$ state splits into two sublevels, 169.8 cm⁻¹ apart from each other, which in the approximation of an axial system would yield $D=84.9~{\rm cm}^{-1}$. Diagonalization of the ZFS and the g-tensor yields eigenvalues and eigenvectors listed in Supplementary Table 8.

VASP calculations of phonons

VASP⁵⁷ calculations on **1**, **1-** d_4 and **1-** d_{18} were conducted . Geometry optimizations were performed on the single-crystal X-ray structure of **1** at 100 K. The optimized structure completed at 0 T was used for the phonon calculations. Spin-polarized, periodic DFT calculations were performed using VASP with the Projector Augmented Wave (PAW)^{58,59} method and the local density approximation (GGA)⁶⁰ + U (U = 5.37)^{58,61} exchange correlation functional. An energy cut off was 900 eV for the plane-wave basis of the valence electrons. Total energy tolerance for electronic structure minimization was 10^{-8} eV. The optB86b-vdW, a non-local correlation functional that approximately accounts for dispersion interactions, was applied⁶². For the structure relaxation, a $1 \times 3 \times 1$ Monkhorst-Pack mesh was applied. Phonopy⁶³, an open source phonon analyzer, was used to create a 140 atom, $1 \times 2 \times 1$ supercell structure. VASP was then employed to calculate the force constants on the supercell in real space using DFT. The crystal structure of **1** has C_{2h} symmetry. Jmol was used to create the Supplementary Movies. Since Raman and far-IR properties of **1** and **1-** d_4 near 115 cm⁻¹ are similar, only the calculated phonons of **1-** d_4 are presented.

Data availability

The crystallographic coordinates for the structures of 1 at 100 K from single-crystal X-ray diffraction and 1-d₁₈ at 4 K from powder neutron diffraction reported in this study have been deposited at the Cambridge Crystallographic Data Centre (CCDC), under deposition numbers CCDC 1842364 and CCDC 1842460, respectively. These data can be obtained free of charge from the Cambridge Crystallographic Data Centre via www.ccdc.cam.ac.uk/data_request/cif.

Code availability

Electronic calculations were conducted with the ORCA code (https://orcaforum.cec.mpg.de/)
which is free for academic use but commercial for industrial use. VASP (Vienna *ab initio* simulation package) for the periodic DFT phonon calculations is available at
https://www.vasp.at/

References

- Benelli, C. & Gatteschi, D. *Introduction to Molecular Magnetism : From Transition Metals to Lanthanides*. (Wiley, 2015).
- Frost, J. M., Harriman, K. L. M. & Murugesu, M. The rise of 3-d single-ion magnets in molecular magnetism: towards materials from molecules? *Chem. Sci.* 7, 2470-2491 (2016).
- 3 Layfield, R. A. Organometallic single-molecule magnets. *Organometallics* **33**, 1084-1099 (2014).
- 4 Krzystek, J. & Telser, J. Measuring giant anisotropy in paramagnetic transition metal complexes with relevance to single-ion magnetism. *Dalton Trans.* **45**, 16751-16763 (2016).
- McInnes, E. J. L. & Winpenny, R. E. P. in *Comprehensive Inorganic Chemistry II* (ed Kenneth Poeppelmeier) 371-395 (Elsevier, 2013).
- Neese, F. & Pantazis, D. A. What is not required to make a single molecule magnet. Faraday Discuss. 148, 229-238 (2011).
- Gao, S., Ed. Molecular Nanomagnets and Related Phenomena. (Springer, 2015).

- 8 Graham, M. J., Zadrozny, J. M., Fataftah, M. S. & Freedman, D. E. Forging solid-state qubit design principles in a molecular furnace. *Chem. Mater.* **29**, 1885–1897 (2017).
- 9 Moreno-Pineda, E., Godfrin, C., Balestro, F., Wernsdorfer, W. & Ruben, M. Molecular spin qudits for quantum algorithms. *Chem. Soc. Rev.* 47, 501-513 (2018).
- Suturina, E. A. *et al.* Magneto-structural correlations in pseudotetrahedral forms of the [Co(SPh)₄]²⁻ complex probed by magnetometry, MCD spectroscopy, advanced EPR techniques, and ab initio electronic structure calculations. *Inorg. Chem.* **56**, 3102-3118 (2017).
- 11 Craig, G. A. & Murrie, M. 3d single-ion magnets. *Chem. Soc. Rev.* 44, 2135-2147 (2015).
- Gatteschi, D. & Sessoli, R. Quantum tunneling of magnetization and related phenomena in molecular materials. *Angew. Chem. Int. Ed.* **42**, 268-297 (2003).
- Dey, M. & Gogoi, N. Geometry-mediated enhancement of single-ion anisotropy: A route to single-molecule magnets with a high blocking temperature. *Angew. Chem. Int. Ed.* **52**, 12780-12782 (2013).
- Boča, R. Zero-field splitting in metal complexes. *Coord. Chem. Rev.* **248**, 757-815 (2004).
- Gómez-Coca, S. *et al.* Origin of slow magnetic relaxation in Kramers ions with non-uniaxial anisotropy. *Nat. Commun.* **5**, 4300 (2014).
- Stavretis, S. E. *et al.* Magnetic transitions in iron porphyrin halides by inelastic neutron scattering and *ab initio* studies of zero-field splittings. *Inorg. Chem.* **54**, 9790-9801 (2015).

- 17 Schnegg, A., Behrends, J., Lips, K., Bittl, R. & Holldack, K. Frequency domain Fourier transform THz-EPR on single molecule magnets using coherent synchrotron radiation.

 Phys. Chem. Chem. Phys. 11, 6820-6825 (2009).
- Brackett, G. C., Richards, P. L., Caughey, W. S. Far-infrared magnetic resonance in Fe(III) and Mn(III) porphyrins, myoglobin, hemoglobin, ferrichrome A, and Fe(III) dithioncarbamates. *J. Chem. Phys.* **54** (1971).
- Brackett, G. C. Far-Infrared Magnetic Resonance in Fe(III) and Mn(III) Porphyrins,

 Myoglobin, Hemoglobin, Ferrichrome A, and Fe(III) Dithiocarbamates Ph. D. thesis,

 University of California, Berkeley, (1970).
- 20 Uenoyama, H. Far-infrared studies on hemin and hemin-like complexes. *Biochim*. *Biophys. Acta* 230, 479-481 (1971).
- Ray, K. *et al.* The electronic structure of the isoelectronic, square-planar complexes $[Fe^{II}(L)_2]^{2-}$ and $[Co^{III}(LBu)_2]^{-}$ (L^{2-} and $(LBu)^{2-}$ = benzene-1,2-dithiolates): An experimental and density functional theoretical study. *J. Am. Chem. Soc.* **127**, 4403-4415 (2005).
- Rechkemmer, Y. *et al.* A four-coordinate cobalt(II) single-ion magnet with coercivity and a very high energy barrier. *Nat. Commun.* **7**, 10467 (2016).
- Jiang, S.-D. *et al.* Direct observation of very large zero-field splitting in a tetrahedral Ni^{II}Se₄ coordination complex. *J. Am. Chem. Soc.* **137**, 12923-12928 (2015).
- 24 Bloor, D. & Copland, G. M. Far infrared spectra of magnetic ions in crystals. *Rep. Prog. Phys.* **35**, 1173-1264 (1972).
- Rechkemmer, Y. *et al.* Comprehensive spectroscopic determination of the crystal field splitting in an erbium single-ion magnet. *J. Am. Chem. Soc.* **137**, 13114-13120 (2015).

- Gnezdilov, V. P., Eremenko, V. V., Peschansky, A. V. & Fomin, V. I. Raman scattering by low-energy electronic excitations of Fe²⁺ ions in ferrous fluosilicate. *Fiz. Nizk. Temp.* (Low Temp. Phys.) 17, 253-258 (1991).
- 27 Champion, P. M. & Sievers, A. I. Far-infrared magnetic resonance in FeSiF₆•6H₂O and Fe(SPh)₄²-. *J. Chem. Phys.* **66**, 1819-1825 (1977).
- 28 Krzystek, J. *et al.* High-frequency and -field EPR and FDMRS study of the [Fe(H₂O)₆]²⁺ ion in ferrous fluorosilicate. *J. Magn. Reson.* **213** (2011).
- Tregenna-Piggott, P. L. W. & Best, S. P. Single-crystal raman spectroscopy of the rubidium alums RbM^{III}(SO₄)₂·12H₂O (M^{III} = Al, Ga, In, Ti, V, Cr, Fe) between 275 and 1200 cm⁻¹: correlation between the electronic structure of the tervalent cation and structural abnormalities. *Inorg. Chem.* **35**, 5730-5736 (1996).
- Spichiger, D. *et al.* Electronic Raman transitions from the vanadium(III) hexa-aqua cation, in guanidinium vanadium sulphate. *Chem. Phys. Lett.* **337**, 391-397 (2001).
- Beaulac, R. *et al.* The electronic ground state of [V(urea)₆]³⁺ probed by NIR luminescence, electronic raman, and high-field EPR spectroscopies. *Inorg. Chem.* **45**, 3399-3407 (2006).
- Carver, G., Spichiger, D. & Tregenna-Piggott, P. L. W. Electronic Raman spectroscopy of the vanadium(III) hexaaqua cation in guanidinium vanadium sulphate: Quintessential manifestation of the dynamical Jahn–Teller effect. *J. Chem. Phys.* **122**, 124511 (2005).
- Tregenna-Piggott, P. L. W. & Carver, G. Structure and bonding of the vanadium(III) hexa-aqua cation. 2. Manifestation of dynamical Jahn–Teller coupling in axially distorted vanadium(III) complexes. *Inorg. Chem.* **43**, 8061-8071 (2004).

- Dobe, C. *et al.* Variable temperature inelastic neutron scattering study of chromium(II)

 Tutton salt: manifestation of the ⁵E⊗e Jahn–Teller effect. *Chem. Phys. Lett.* **362**, 387-396 (2002).
- Tregenna-Piggott, P. L. W. & Güdel, H.-U. Influence of Jahn-Teller coupling on the magnetic properties of transition metal complexes with orbital triplet ground terms: magnetization and electronic raman studies of the titanium(III) Hexa-Aqua Cation. *Inorg. Chem.* **40**, 5497-5506 (2001).
- Orbach, R. & Stapleton, H. J. in *Electron Paramagnetic Resonance* (ed S. Geschwind) 121-216 (Plenum Press, 1972).
- 37 Schwoerer, M. & Wolf, H. C. in *Organic Molecular Solids* Ch. 5, 89-124 (Wiley-VCH, 2008).
- Lunghi, A., Totti, F., Sanvito, S. & Sessoli, R. Intra-molecular origin of the spin-phonon coupling in slow-relaxing molecular magnets. *Chem. Sci.* **8**, 6051-6059 (2017).
- Escalera-Moreno, L., Suaud, N., Gaita-Ariño, A. & Coronado, E. Determining key local vibrations in the relaxation of molecular spin qubits and single-molecule magnets. *J. Phys. Chem. Lett.* **8**, 1695-1700 (2017).
- 40 Goodwin, C. A. P., Ortu, F., Reta, D., Chilton, N. F. & Mills, D. P. Molecular magnetic hysteresis at 60 kelvin in dysprosocenium. *Nature* **548**, 439-442 (2017).
- Frediani, P., Rovai, D., Muniz-Miranda, M., Salvini, A. & Caporali, M. An easy way to perdeuterated pyrazoles by catalytic exchange reactions. *Catal. Commun.* **2**, 125-128 (2001).
- 42 Cohen-Tannoudji, C., Diu, B. & Laloe, F. *Quantum Mechanics*. Vol. 2 1078, 1066 and 1313 (Wiley, 1977).

- 43 Cotton, F. A. Chemical Applications of Group Theory. p. 303 (Wiley, 1990).
- 44 Koster, G. F., Dimmock, J. O., Wheeler, R. G. & Statz, H. *Properties of the Thirty-Two Point Groups*. (MIT Press, 1963).
- Jacobs, P. W. M. *Group Theory with Applications in Chemical Physics*. (Cambridge University Press, 2005).
- 46 Pilbrow, J. R. Effective g values for S = 3/2 and S = 5/2. J. Magn. Reson. **31**, 479-490 (1978).
- Gast, P. & Groenen, E. J. J. EPR Interactions g-Anisotropy. *eMagRes* **5**, 1435–1444 (2016).
- 48 Cohen-Tannoudji, C., Laloë, F. & Diu, B. *Quantum Mechanics*. Vol. 1 405-415 (Wiley, 1977).
- 49 Brinzari, T. V. *et al.* Electron-phonon and magnetoelastic interactions in ferromagnetic Co[N(CN)₂]₂. *Phys. Rev. Lett.* **111**, 047202 (2013).
- Lohr, L. L., Miller, J. C. & Sharp, R. R. Electronic structure and magnetic properties of high-spin octahedral Co(II) complexes: Co(II)(acac)₂(H₂O)₂. *J. Chem. Phys.* **111**, 10148-10158 (1999).
- Bencini, A., Benelli, C., Gatteschi, D. & Zanchini, C. ESR spectra of low-symmetry high-spin cobalt(II) complexes. 6,6-Methylquinoline, pyridine, and water adducts of cobalt(II) acetylacetonate. *Inorg. Chem.* **19**, 3027-3030 (1980).
- Görller-Walrand, C. & Binnemans, K. Spectral intensities of f-f transitions. *Handbook on the Physics and Chemistry of Rare Earths* **25**, 101-264 (1998).
- Rinehart, J. D. & Long, J. R. Exploiting single-ion anisotropy in the design of f-element single-molecule magnets. *Chem. Sci.* **2**, 2078-2085 (2011).

- Clark, R. J. H. & Dines, T. J. in *Advances in Infrared and Raman Spectroscopy, Vol. 9* (eds R. J. H. Clark & R. E. Hester) Ch. 5, 282-360 (Heyden & Son, 1982).
- Frediani, P., Rovai, D., Muniz-Miranda, M., Salvini, A. & Caporali, M. An easy way to perdeuterated pyrazoles by catalytic exchange reactions. *Catal. Commun.* **2**, 125-128 (2001).
- Kresse, G. & Furthmüller, J. Efficient iterative schemes for ab initio total-energy calculations using a plane-wave basis set. *Phys. Rev. B* **54**, 11169-11186 (1996).
- Kresse, G. & Joubert, D. From ultrasoft pseudopotentials to the projector augmentedwave method. *Phys. Rev. B* **59**, 1758-1775 (1999).
- 58 Blöchl, P. E. Projector augmented-wave method. *Phys. Rev. B* **50**, 17953-17979 (1994).
- 59 Perdew, J. P., Burke, K. & Ernzerhof, M. Generalized gradient approximation made simple. *Phys. Rev. Lett.* **77**, 3865-3868 (1996).
- Zhou, F., Cococcioni, M., Marianetti, C. A., Morgan, D. & Ceder, G. First-principles prediction of redox potentials in transition-metal compounds with LDA + U. *Phys. Rev. B* 70, 235121 (2004).
- Klimeš, J., Bowler, D. R. & Michaelides, A. Chemical accuracy for the van der Waals density functional. *J. Phys. Condens. Matter* **22**, 022201 (2010).
- Togo, A. & Tanaka, I. First principles phonon calculations in materials science. *Scr. Mater.* **108**, 1-5 (2015).

Acknowledgment

The authors thank financial support by the US National Science Foundation (CHE-1633870 to Z-L.X.), U.S. Department of Navy HBCU/MI program (K.T.), Deutsche Forschungsgemeinschaft

and Max-Planck-Gesellschaft (M.A., E.B. and F.N.), and a Shull Wollan Center Graduate Research Fellowship (S.E.S). Acknowledgment is also made to the Donors of the American Chemical Society Petroleum Research Fund for partial support of this work. Computational resources for the VASP DFT calculations were made available through the VirtuES and ICE-MAN projects, funded by the Laboratory Directed Research and Development at Oak Ridge National Laboratory. The NHMFL is supported by NSF through NSF-DMR-0084173 and the State of Florida. Partial funding for open access to this article was provided by the University of Tennessee's Open Publishing Support Fund. Z-L.X. thanks Michael O. Yokosuk, Ryan A. Wallace, and Profs. Janice L. Musfeldt and Michael J. Sepaniak for their help.

Author contributions

D.H.M. synthesized and characterized the complexes. D.H.M, K.T. and Z.L. performed and interpreted the Raman experiments. D.H.M., M.O., J.L. and D.S. performed and interpreted the far-IR experiments. A.J.R-C., Y.C. L.L.D. and S.E.S. conducted the phonon calculations. M.A., F.N. and E.B. developed the vibronic model, simulated positions of Kramers doublets with magnetic fields, and performed electronic structure calculations. A.P. calculated the intensities of the IR phonon modes. A.C.L. and D.H.M. performed the single-crystal structure determination of 1 by X-ray diffraction. C.M.B. performed the structure determination of 1-d₁₈ by powder neutron diffraction. Z-L.X. designed and supervised the research and helped analyses of spectroscopic data. D.H.M., S.E.S., M.A., E.B. and Z-L.X. wrote the manuscript with input from all authors.

Supplemental information accompanies this paper at http://

Competing interests. The authors declare no competing interests.

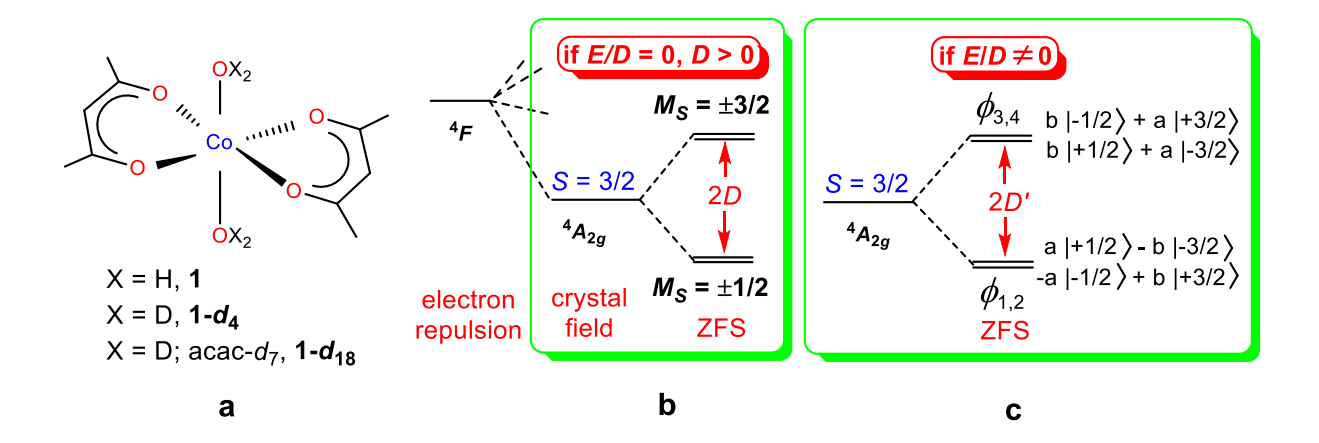
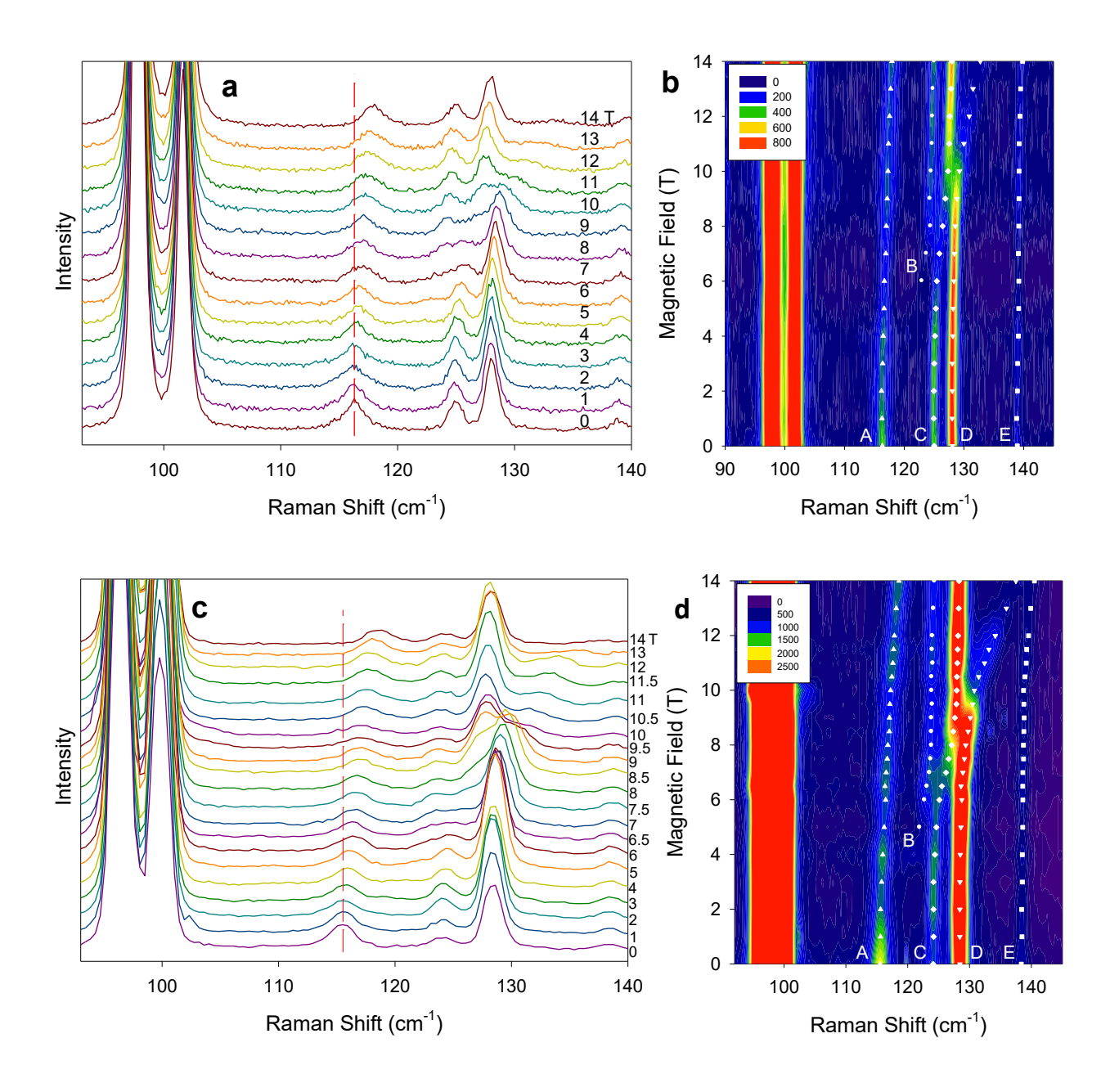


Figure 1 | 1, 1- d_4 and 1- d_{18} and their ZFS

(a) Structures of 1, 1-d₄ and 1-d₁₈. (b) Ground-state quartet levels in high-spin, d⁷ complexes with D_{4h} symmetry (D > 0; E/D = 0). (c) The quartet levels in 1 with lower symmetry $[E/D \neq 0, D' = (D^2 + 3E^2)^{1/2}]$, where the mixing coefficients $a = \cos \beta$ and $b = \sin \beta$ are described by the mixing angle β obtained from the spin Hamiltonian (S = 3/2) with large D in the absence of field^{46,47}. Mixing depends on the rhombicity as $\tan 2\beta = \sqrt{3}$ (E/D) (SI of ref. 15).



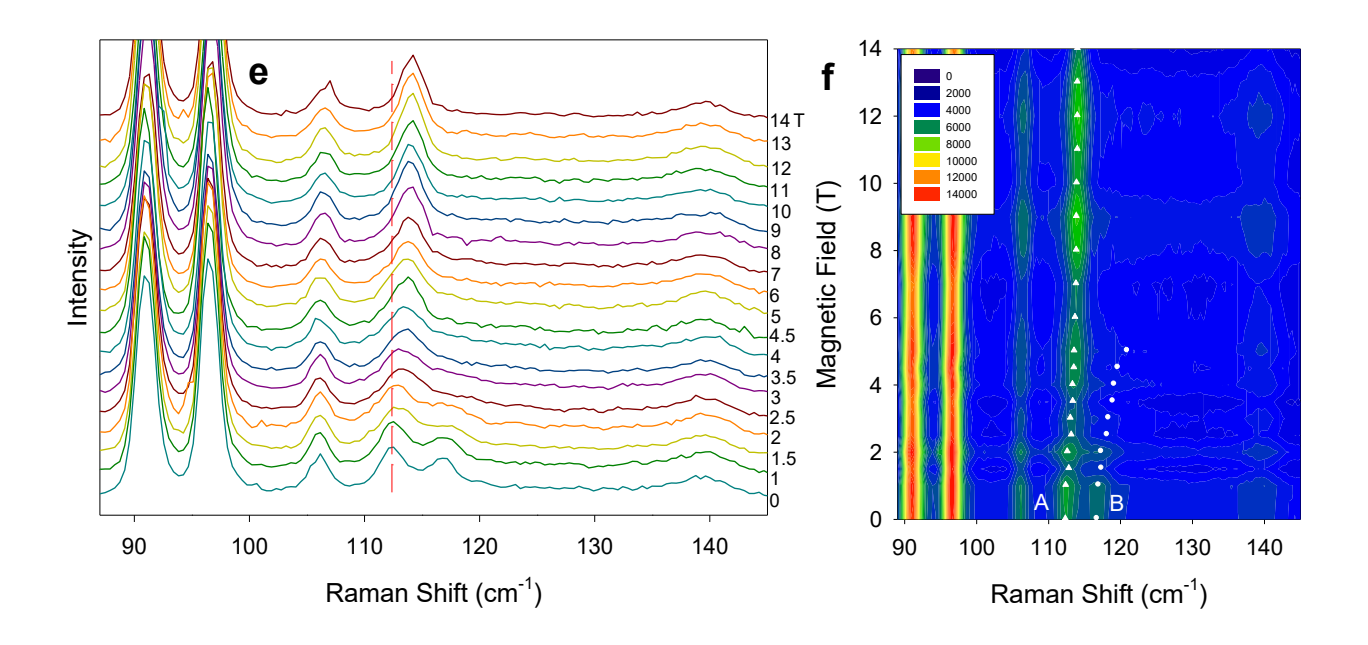


Figure 2 | Raman spectra and contour maps in 0-14 T magnetic fields

(a-b) 1, (c-d) 1-d₄ and (e-f) 1-d₁₈. Vertical lines indicate Peak A as one spin-phonon coupled peak in each set of spectra. The contour maps more clearly show the avoided crossings as a result of the spin-phonon couplings. The color codes in (b, d, f) are in units of counts. Raman spectra of 1 were collected up to 18 T but were trimmed to be consistent with other data sets.

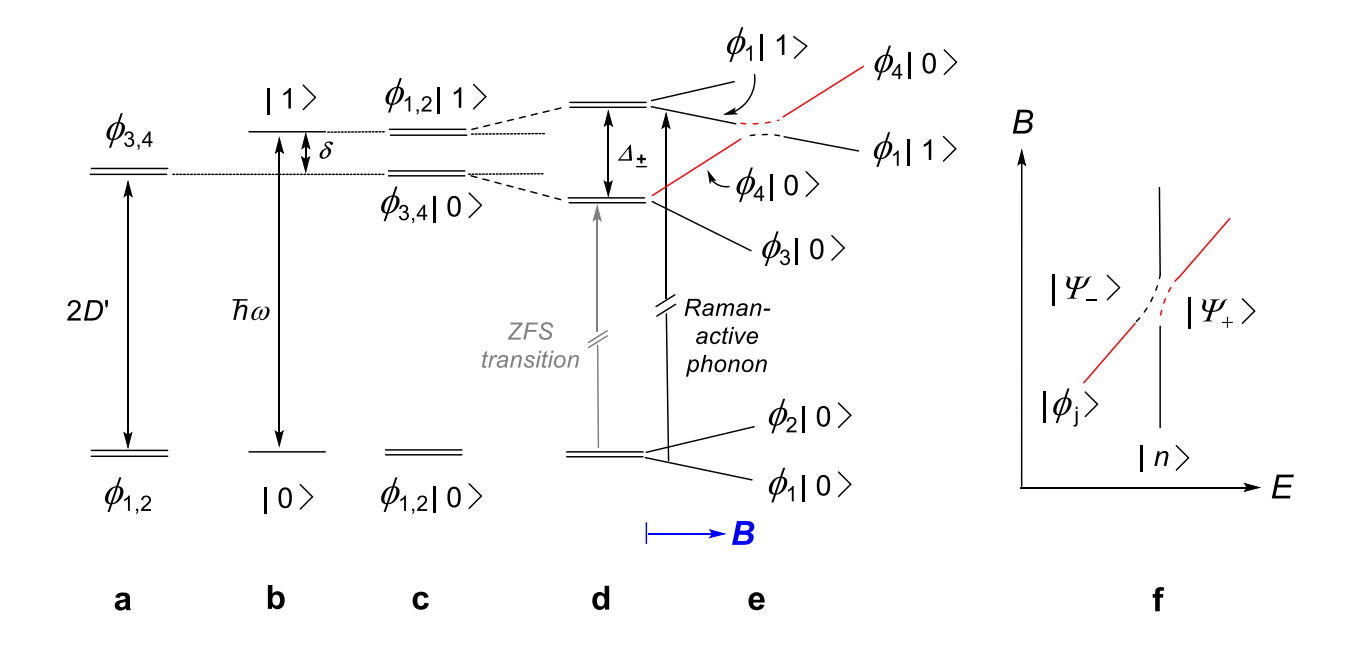


Figure 3 | Schematic view of the spin-phonon coupling

(a) Zero-field splitting 2D' of the magnetic/spin quartet ground state (with eigenfunctions in Figure 1c when no field is applied; Off-axis field induces additional m_s mixing). (b) Vibrational states of a selected phonon with eigenfunctions $|0\rangle$ and $|1\rangle$ and a small energy separation δ above the excited KD $\phi_{3,4}$. (c) Spin-phonon product states with product functions $\phi_i|n\rangle$ still without vibronic coupling. (d) Vibronic coupling with coupling constant Λ , leading to an energy shift and splitting: $\Delta_{\pm} = (\delta^2 + \Lambda^2)^{1/2}$. The ZFS transition (in grey color) is vanishingly weak in Raman, because it is only magnetic-dipole-allowed. (e) Zeeman splitting of vibronic states in a field B and avoided crossing from the coupling between the $\phi_4|0\rangle$ and $\phi_1|1\rangle$ states. Note the states $\phi_{1,2}|0\rangle$ and $\phi_{1,2}|1\rangle$ have pairwise identical slopes, whereas $\phi_{1,2}|0\rangle$ and $\phi_{3,4}|0\rangle$ have different slopes. The net transition from the lowest level $\phi_1|0\rangle$ to $\phi_1|1\rangle$ is in essence a phonon excitation and thus Raman-allowed (black arrow), and it is field-independent. When $\phi_4|0\rangle$, the upper magnetic level of the excited electronic KD, approaches $\phi_1|1\rangle$, additional coupling occurs, leading to a field-

dependent transition. The ZFS transitions in (d) are vanishingly weak in Raman spectra, because they are only magnetic-dipole-allowed. The same holds for the $\phi_1|0\rangle \rightarrow \phi_3|0\rangle$, $\phi_1|0\rangle \rightarrow \phi_4|0\rangle$, and $\phi_1|0\rangle \rightarrow \phi_2|1\rangle$ transitions, which are not marked in (e). (Transitions from the first excited level, $\phi_2|0\rangle$, are neglected because of vanishing thermal population at 1.5-5 K.) (f) Avoided crossing in the Raman spectra based on Equation (2). The red branches are weak in Raman intensity and only partially visible because they represent quasi-pure magnetic-dipole transitions.

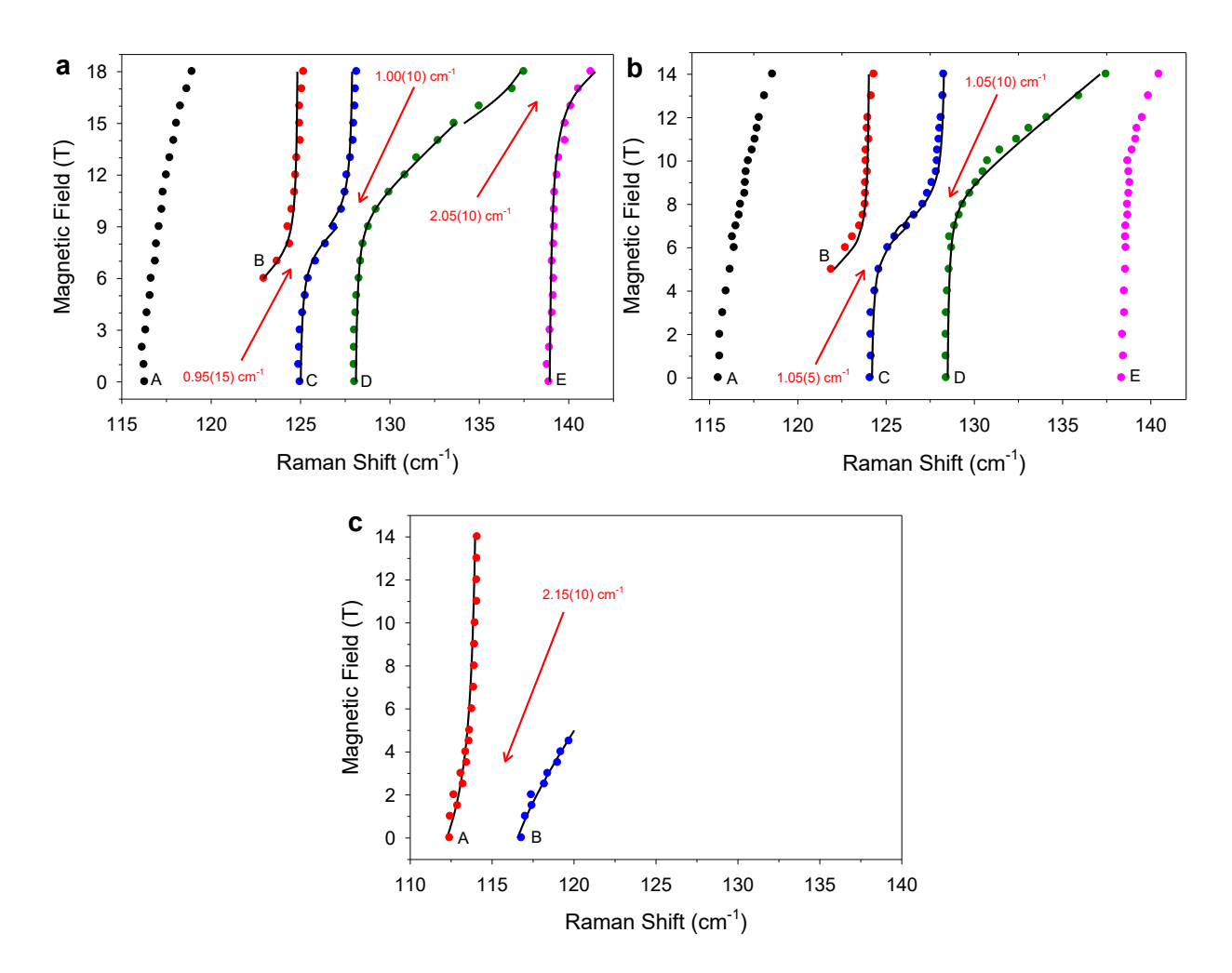


Figure 4 | Peak positions vs. magnetic fields for selected transitions in the Raman spectra (a) 1; (b) 1- d_4 ; (c) 1- d_{18} . The solid lines are fittings using Equation (2), giving the coupling constants |A|. Arrows point to corresponding avoided crossings for |A|.

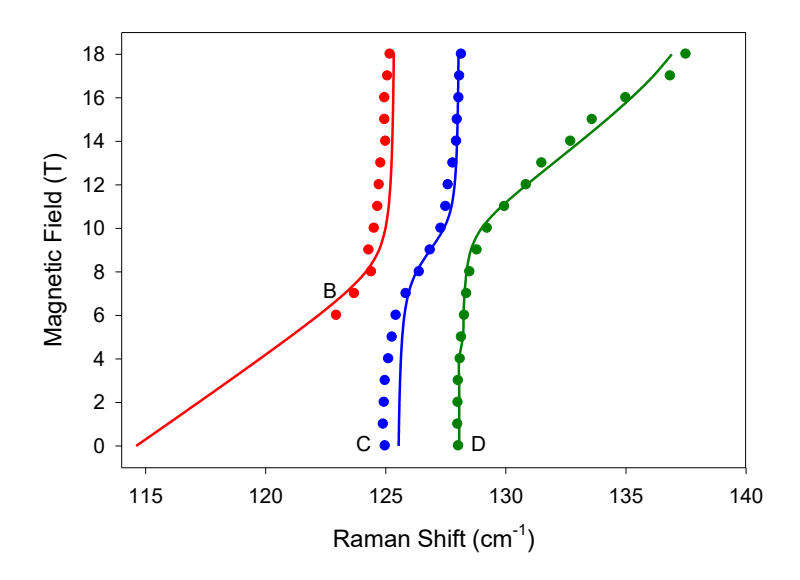


Figure 5 | Fitting of Raman spectra

Simulated (solid lines) and experimental (circles) positions of field-dependent (B|z) Raman transitions corresponding to peaks B (red), C (blue) and D (green) of **1**. $g_z = 1.49$, $\hbar \omega_1 = 125.4$ cm⁻¹, $\hbar \omega_2 = 128.1$ cm⁻¹, $\hbar \omega_3 = 139.5$ cm⁻¹ (not shown in the figure); $E_1 = 1.14$ cm⁻¹, $E_2 = 0.88$ cm⁻¹, $E_3 = 2.66$ cm⁻¹ [E/D = 0.17 (ORCA NEVPT2); $E_1 = 1.15$ cm⁻¹]. $E_1 = 1.14$ cm⁻¹, $E_2 = 0.88$ cm⁻¹, $E_3 = 2.66$ cm⁻¹ [E/D = 0.17 (ORCA NEVPT2); $E_1 = 1.15$ cm⁻¹]. $E_1 = 1.14$ cm⁻¹, $E_2 = 0.88$ cm⁻¹, $E_3 = 2.66$ cm⁻¹ [E/D = 0.17 (ORCA NEVPT2); $E_1 = 1.15$ cm⁻¹]. $E_1 = 1.14$ cm⁻¹, $E_2 = 0.88$ cm⁻¹, $E_3 = 2.66$ cm⁻¹ [E/D = 0.17 (ORCA NEVPT2); $E_1 = 1.15$ cm⁻¹]. $E_1 = 1.14$ cm⁻¹, $E_2 = 0.88$ cm⁻¹, $E_3 = 2.66$ cm⁻¹ [E/D = 0.17 (ORCA NEVPT2); $E_1 = 1.15$ cm⁻¹]. $E_1 = 1.14$ cm⁻¹, $E_2 = 0.88$ cm⁻¹, $E_3 = 2.66$ cm⁻¹ [E/D = 0.17 (ORCA NEVPT2); $E_1 = 1.15$ cm⁻¹]. $E_1 = 1.14$ cm⁻¹, $E_2 = 0.88$ cm⁻¹, $E_3 = 2.66$ cm⁻¹ [E/D = 0.17 (ORCA NEVPT2); $E_1 = 1.15$ cm⁻¹]. $E_1 = 1.14$ cm⁻¹, $E_2 = 0.88$ cm⁻¹, $E_3 = 2.66$ cm⁻¹ [E/D = 0.17 (ORCA NEVPT2); $E_1 = 1.15$ cm⁻¹]. $E_1 = 1.14$ cm⁻¹, $E_2 = 0.88$ cm⁻¹, $E_3 = 0.88$ cm⁻¹,

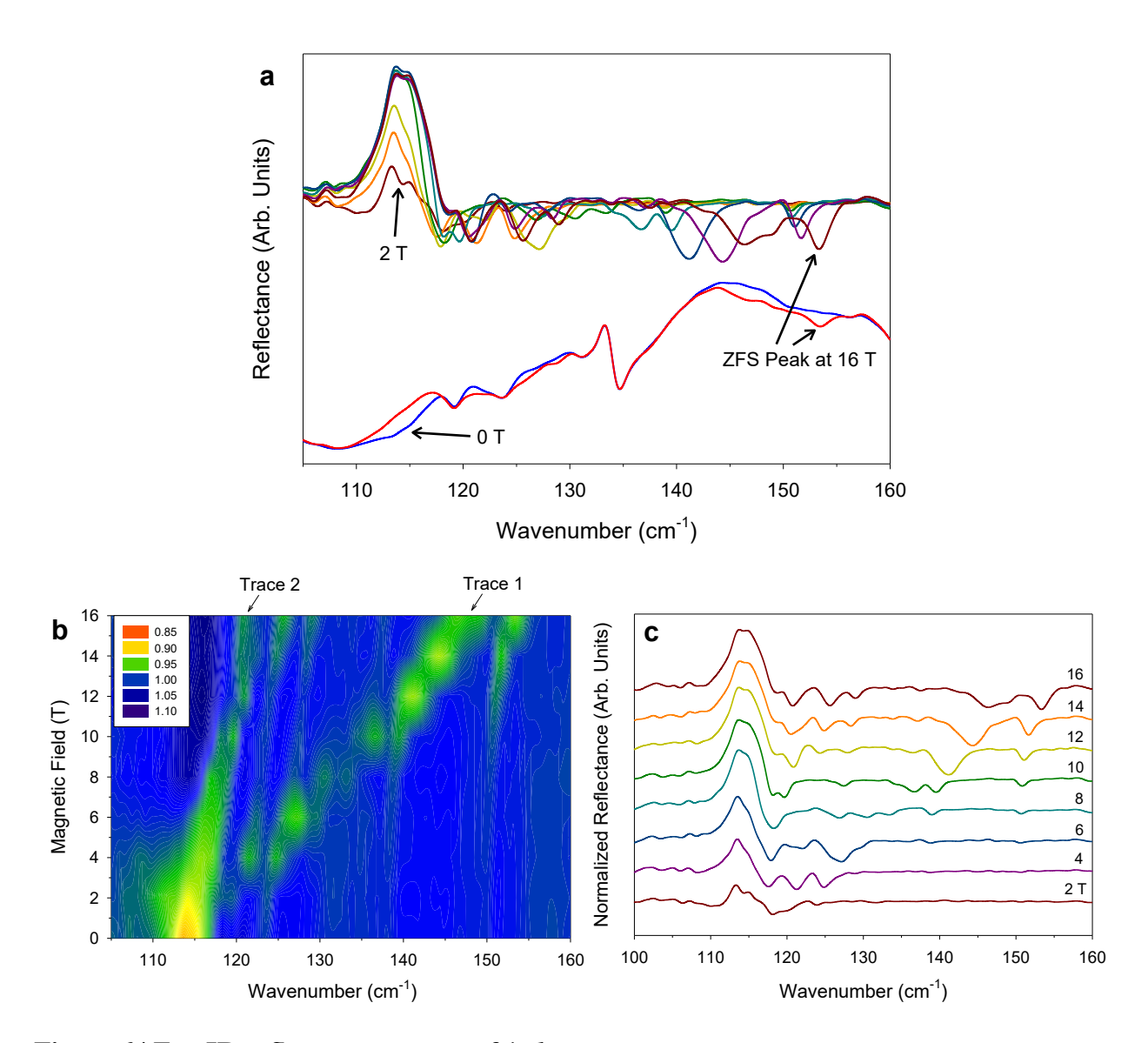


Figure 6 | Far-IR reflectance spectra of 1-d4

(a) Reflectance spectra (Bottom, 0 T-blue and 16 T-red) and normalized (by the 0 T) reflectance spectra (Top) by a single crystal of **1-d₄**, in which the ZFS transition is more visible as it shifts with field at 2, 4, 6, 8, 10, 12, 14 and 16 T. (b) Contour plot of the normalized reflectance spectra (by the average of all spectra) which shows the ZFS transitions and the magnetic features of spin-phonon coupled peaks. (c) Normalized reflectance spectra using data in (a).

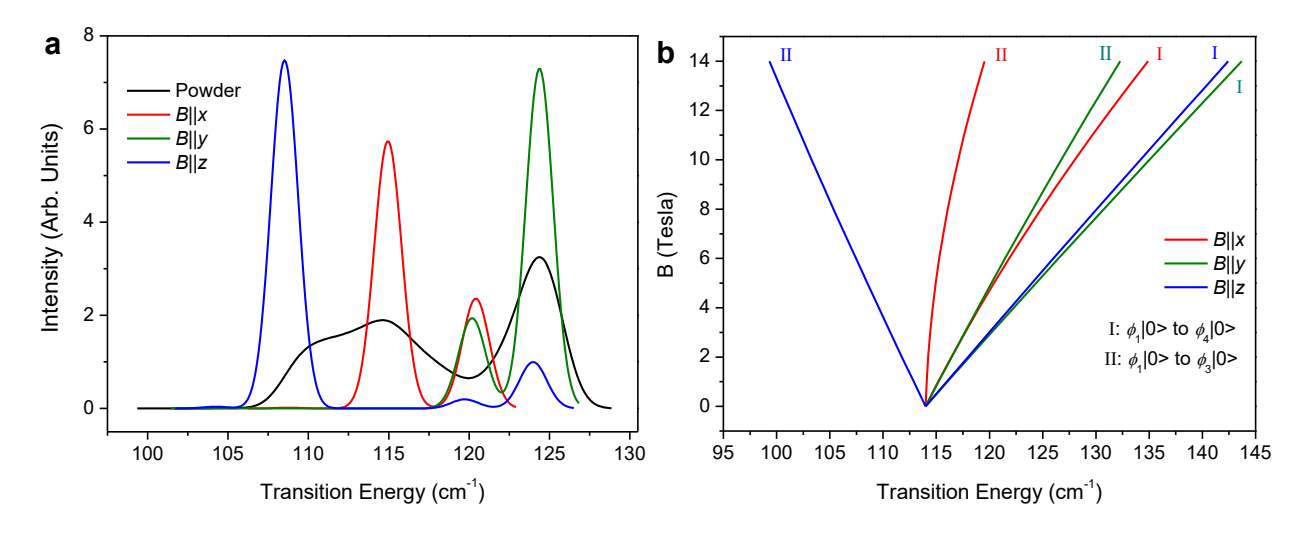


Figure 7 | Simulated inter-KD, magnetic-dipole-allowed transitions and their field dependence

(a) Simulated inter-KD, magnetic-dipole-allowed transitions for the S = 3/2, spin-only Hamiltonian description of **1**. Single-crystal spectra for fields of 5 T in x, y, z directions at 1.7 K are shown in red, green, and blue. The powder average is given in black. Vibronic coupling was ignored. Spin-Hamiltonian parameters are taken from ref. 15: D = 50.2 cm⁻¹, E/D = 0.31, $g_x = 2.50$, $g_y = 2.57$, $g_z = 2.40$ (corresponding g'-values for ground and excited KDs: g'i(1) = 2.65, 6.95, 1.83; and g'i(2) = 2.34, 1.80, 6.63, respectively). The dominant pairs of left and right lines found for the single-crystal orientations (in blue, green, red) correspond to the dominant $\phi_1|0\rangle \rightarrow \phi_2|0\rangle$ and $\phi_1|0\rangle \rightarrow \phi_4|0\rangle$ transitions, respectively. (b) Field dependence of the inter-KD spectra for fields in x, y, z directions.